Tubulin lattice in cilia is in a stressed form regulated by microtubule inner proteins

Muneyoshi Ichikawa[a,1,2], Ahmad Abdelzaher Zaki Khalifa[a,1], Shintaroh Kubo[b], Daniel Dai[a], Kaustuv Basu[c], Mohammad Amin Faghfor Maghrebi[a], Javier Vargas[a], and Khanh Huy Bui[a,3]

[a]Department of Anatomy and Cell Biology, McGill University, Montréal, QC H3A 0C7, Canada; [b]Department of Biophysics, Graduate School of Science, Kyoto University, 606-8502 Kyoto, Japan; and [c]Facility for Electron Microscopy Research, McGill University, Montréal, QC H3A 0C7, Canada

Edited by Takashi Ishikawa, Paul Scherrer Institut (PSI), Villigen PSI, Switzerland, and accepted by Editorial Board Member Yale E. Goldman August 22, 2019 (received for review July 2, 2019)

Cilia, the hair-like protrusions that beat at high frequencies to propel a cell or move fluid around are composed of radially bundled doublet microtubules. In this study, we present a near-atomic resolution map of the *Tetrahymena* doublet microtubule by cryoelectron microscopy. The map demonstrates that the network of microtubule inner proteins weaves into the tubulin lattice and forms an inner sheath. From mass spectrometry data and de novo modeling, we identified Rib43a proteins as the filamentous microtubule inner proteins in the protofilament ribbon region. The Rib43a–tubulin interaction leads to an elongated tubulin dimer distance every 2 dimers. In addition, the tubulin lattice structure with missing microtubule inner proteins (MIPs) by sarkosyl treatment shows significant longitudinal compaction and lateral angle change between protofilaments. These results are evidence that the MIPs directly affect and stabilize the tubulin lattice. It suggests that the doublet microtubule is an intrinsically stressed filament and that this stress could be manipulated in the regulation of ciliary waveforms.

microtubule | ciliopathies | cryoelectron microscopy | cilia | axoneme

Microtubules are tubular structures composed of protofilaments (PFs) of α- and β-tubulin heterodimers in eukaryotes. Microtubules are responsible for structural support, tracks in intracellular transport, and organization of organelles. In the cilia, 9 doublet microtubules (doublets) are radially bundled to form an axonemal structure. The doublet is made up of a complete 13-PF A-tubule and an incomplete 10-PF B-tubule (Fig. 1*A*). The doublet is the scaffold where ciliary proteins, such as axonemal dyneins and radial spokes, are periodically docked (1). These proteins are important to initiate and regulate the bending motion of the cilia. The doublet also serves as the tracks for motor proteins kinesin-2 and dynein-2 carrying intraflagellar transport cargoes toward the distal tip and back (2). Defects in ciliary proteins cause abnormal motility and function, hence, leading to cilia-related diseases, such as primary ciliary dyskinesia and Bardet-Biedl syndrome (3).

In contrast to the singlet microtubule (singlet) that shows cycles of growth and shrinkage called dynamic instability (4), the doublet is highly stable both in vivo and ex vivo (5). In particular, the PF ribbon region, i.e., the shared region between the A- and B-tubules (Fig. 1*A*), is stable even after high concentration of sarkosyl treatment (6, 7). In the lumen of the doublet, microtubule inner proteins (MIPs) bind with a 48-nm periodicity to the tubulin lattice as shown by cryoelectron tomography (8–11). Subnanometer structure of the isolated doublet by cryo-electron microscopy (cryo-EM) revealed many new MIPs forming an inner sheath inside the doublet. This inner sheath is composed of different classes of MIPs such as globular and filamentous MIPs (fMIPs). The fMIPs are composed of long α-helices running between the inner ridges of neighboring PF pairs (5). It is possible that these MIPs can exert their effects on the inherent properties of the doublet such as stability, rigidity, and damage resistance. This is similar to how microtubule-associated proteins affect the properties of singlets.

So far, there are not many well-characterized MIPs. Tektin isoforms in sea urchin sperm flagella are the first characterized PF ribbon proteins (6). Rib43a, a 43-kDa protein is another PF ribbon candidate identified in the flagella of the green algae *Chlamydomonas reinhardtii*. However, the exact location of both tektin and Rib43a is unknown. Recently, Rib72a and Rib72b were characterized as components of MIPs inside the A-tubule of *Tetrahymena thermophila* (12). Rib72a/b knockout causes a reduction in swimming speed. FAP45 and FAP52 are MIPs in the B-tubule of *Chlamydomonas* (13). The B-tubules of FAP45 and FAP52 double knockout mutants in *Chlamydomonas* are prone to depolymerization. All these MIPs mentioned above are conserved in humans (14). Mutations in homologs of tektin, Rib72, and FAP52 are associated with diseases in humans (15–17). Therefore, the MIPs must be important for the motility and stability of the cilia.

To date, there are no studies that reveal how MIPs affect the tubulin lattice at the molecular level. In this study, we obtained near-atomic resolution maps of the doublet and the A-tubule from *Tetrahymena* to understand the influence of MIPs on the tubulin lattice. In addition, we have revealed the molecular mechanism of how Rib43a induces changes in the tubulin lattice.

Significance

Here, we present the near-atomic resolution structure of the ex vivo doublet microtubule. This offers new insight into the intricacy of the in vivo tubulin lattice. Unlike the in vitro reconstituted singlet microtubule, the doublet tubulin lattice exhibits highly heterogeneous conformations and lateral curvatures due to the weaving network of microtubule inner proteins. We also reveal the molecular mechanism of how Rib43a proteins bind inside the lumen and induce significant changes in the tubulin lattice. This native protein is directly observed to bind to the taxane-binding pocket of tubulin, similarly to the anticancer drug taxol.

Author contributions: M.I. and K.H.B. designed research; M.I., A.A.Z.K., S.K., and K.B. performed research; J.V. contributed new reagents/analytic tools; M.I., A.A.Z.K., S.K., D.D., M.A.F.M., and K.H.B. analyzed data; and M.I., A.A.Z.K., D.D., and K.H.B. wrote the paper.

The authors declare no conflict of interest.

This article is a PNAS Direct Submission. T.I. is a guest editor invited by the Editorial Board.

Data deposition: The electron microscopy maps of the doublet, sonicated A-tubule and sarkosyl A-tubule are available in the EMDataResource Bank (https://www.emdataresource.org) under accession nos. EMD-20602, EMD-20603, and EMD-20606. The coordinates of tubulin lattice, Rib43a-S and Rib43a-L are available in Protein Data Bank under accession nos. 6U0H, 6U0T, and 6U0U.

[1]M.I. and A.A.Z.K. contributed equally to this work.

[2]Present address: Department of Systems Biology, Graduate School of Biological Sciences, Nara Institute of Science and Technology, Ikoma, Nara 630-0192, Japan.

[3]To whom correspondence may be addressed. Email: huy.bui@mcgill.ca.

This article contains supporting information online at www.pnas.org/lookup/suppl/doi:10.1073/pnas.1911119116/-/DCSupplemental.

First published September 16, 2019.

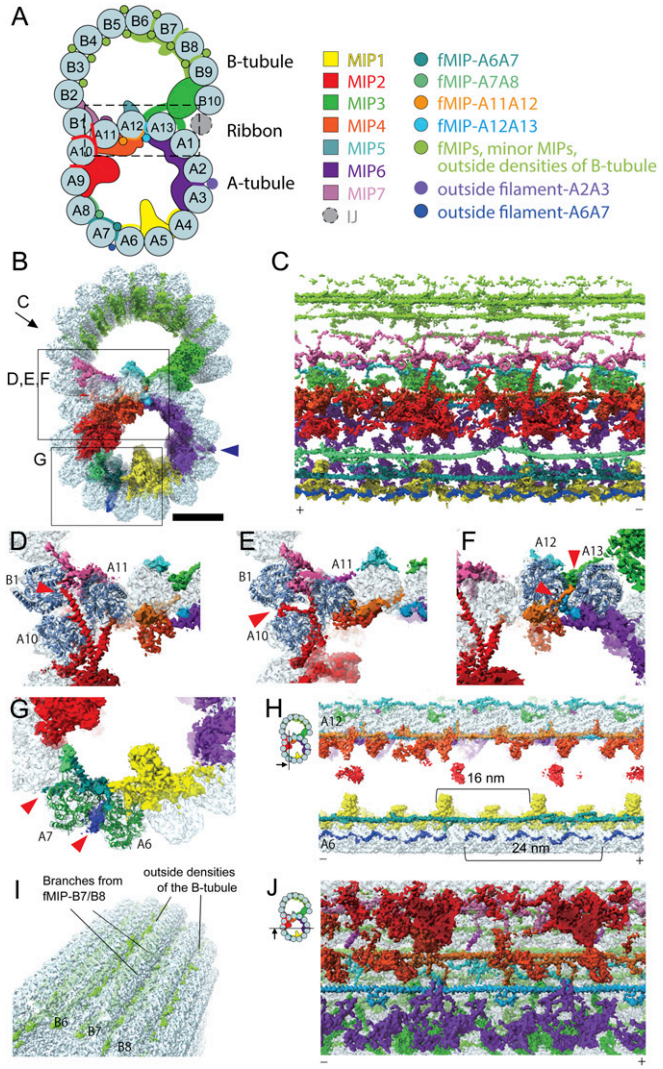

Fig. 1. Networks of the MIPs are woven into the tubulin lattice. (*A*) Schematic cartoon of the doublet from *Tetrahymena* viewed from the tip of the cilia. PF numbers are shown, and MIPs are colored as on the *Right*. The PF ribbon region is indicated as the dashed box. The inner junction (IJ), not presented in our structure, is known to bridge the B- and A-tubules (60). (*B*) Surface rendering of the 48-nm unit of the doublet is colored according to *A*. Blue arrowhead indicates the outside filament-A2A3/the outside molecular ruler (19). (Scale bar, 10 nm.) Views of *C*–*G* are indicated in *B*. (*C*) The weaving network of MIPs inside the tubulin lattice with tubulin densities removed. Plus and minus ends are indicated by (+) and (–) signs, which are consistent throughout. (*D*–*G*) Insertions of the MIPs into the tubulin lattice. Red arrowheads indicate the insertion densities. (*D*) α-Helical branches from the MIP2 go in between PFs A10 and A11. (*E*) A branch of MIP2 (red arrowhead) goes in between PF pairs A10/A11 and A10/B1, reaching outside the tubulin lattice. (*D* and *E*) Cross-sections with different depths along the longitudinal axis of the doublet. (*F*) Branches from fMIPs-A11A12 and -A12A13 (red arrowheads) go in between the tubulin lattice. (*G*) Branches from fMIP-A6A7 reach the outside surface and contact densities outside (red arrowheads). (*H*) Sectional view showing the outside filament-A6A7 (blue). Outside filament-A6A7 appears as a 24-nm repeating unit. (*I*) Outside densities of the B-tubule. (*J*) fMIPs appear as single α-helical structures running in between the inner ridges of the PF pairs A11/A12 and A12/A13. The globular MIPs and fMIPs are connected by branches.

Results

The MIPs Form a Weaving Network with the Tubulin Lattice. To gain insight into the molecular architecture of the *Tetrahymena* doublet, we obtained a cryo-EM map of the 48-nm repeating unit at 4.3-Å resolution (Fig. 1 *A* and *B* and *SI Appendix*, Fig. S1). This map reveals the intricacy of MIPs inside the doublet at a near-atomic level (Fig. 1 *B*–*J* and Movie S1). Even though each designated MIP density in Fig. 1 *A* and *B* contain multiple polypeptides, they are named and colored based on our previous work (5) (Fig. 1*A*).

Instead of simply binding on the luminal surface of the doublet, MIPs consist of many branches, which weave into the tubulin lattice (Fig. 1 *C*–*G*). For instance, the previously identified MIP2 density consists of 2 long α-helices that extend from the inside of the A-tubule to the lumen of the B-tubule (Fig. 1 *C* and *D*). These helices appear to connect with densities from MIP7 at the outer junction.

MIP branches can lace through the A- and B-tubules to the outside of the doublet, a phenomenon that has never been observed with other microtubule-associated proteins. For instance, a part of MIP2 reaches through the lateral gap of PFs A10, A11, and B1 to the outside (Fig. 1*E* and Movie S1). The branch of fMIP-A6A7 also weaves through the tubulin lattice and comes into contact with the outside filament-A6A7 (red arrowhead in Fig. 1*G*). It is possible that the outside filament-A6A7 is a part of the outer dynein arm complex (18) due to its proximity and matching periodicity (24 nm) (Movie S1). This suggests that there is a coordination between proteins inside and outside of the doublet.

Outside the B-tubule, there are many globular densities in the grooves between PFs B3 to B9. These densities are either protrusions from the fMIPs or densities binding outside (Fig. 1 *A*, *B*, and *I* and Movie S1). However, this region has a lower signal-to-noise ratio due to lower resolution than the rest of the doublet (*SI Appendix*, Fig. S1*F*).

The previously described molecular ruler, referred to as "outside filament-A2A3" (Fig. 1*B*, blue arrowhead) has been shown to determine the periodicity of axonemal proteins on the surface of the doublet (19). However, we did not observe any connections between the MIPs and outside filament-A2A3.

The weaving network of MIPs is more complex in the A-tubule than the B-tubule. The A-tubule consists of laterally connected globular MIPs and fMIPs, while the B-tubule contains mainly fMIPs with fewer lateral contacts (Fig. 1 *B*, *C*, and *J*). After sonication, singlet A-tubules with their B-tubule physically broken were observed together with doublet fragments (*SI Appendix*, Fig. S1 *A* and *C*). Treatment of the doublet with 0.2% sarkosyl disintegrated the B-tubule but not the A-tubule (*SI Appendix*, Fig. S1 *A*, *B*, and *D*). The higher stability of the A-tubule compared to the B-tubule (20) may be attributed to such MIP interactions. This illustrates the importance of the MIPs in stabilizing the tubulin lattice.

The PF Ribbon Region Displays a Bimodal Pattern of Tubulin Dimer Distances. One unique feature of the doublet map is that it contains a 48-nm periodicity defined by the MIPs. We clearly distinguished α- and β-tubulins in the map and therefore, confirmed the microtubule seam between PFs A9 and A10 (*SI Appendix*, Fig. S2 *A*–*C*). There are variations in dimer distances among PFs (Fig. 2 *C* and *D*). This heterogeneity even extends to the dimer distances within the same PF. This leads to an extremely heterogenous tubulin lattice relative to the singlet (Fig. 2 *A*–*E*). This should be a direct result of the weaving network of MIPs lacing into the tubulin lattice at different locations.

The lattice length of the B-tubule is slightly shorter than the A-tubule as in Fig. 2*D*. The averaged dimer distance in the B-tubule is 82.4 Å, which translates as being 0.78% shorter compared to the A-tubule (83.1 Å). Since there are fewer MIPs in the B- than the A-tubule, this observation can be explained by the number of MIP insertions into the tubulin lattice. Indeed, the B-tubule was previously proposed to be shorter than the A-tubule, as the doublet

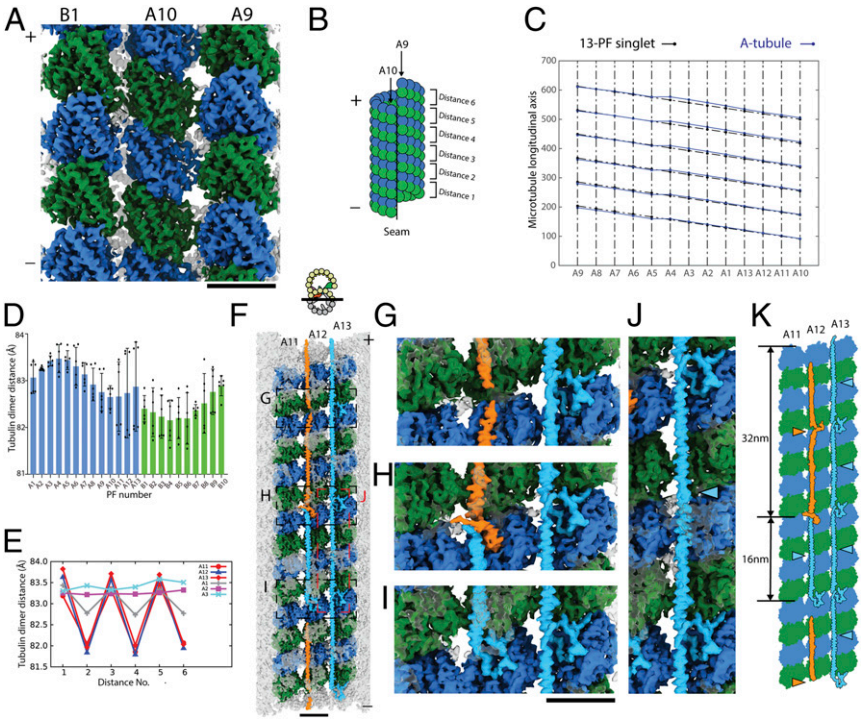

Fig. 2. The complex tubulin lattice within the 48-nm repeating unit of the doublet. (*A*) Outside view of surface rendering of the doublet at PFs A9, A10, and B1. α- and β-tubulins are colored green and blue. (*B*) Schematic diagram of the A-tubule and the tubulin dimer distance measurement. (*C*) Two-dimensional plot of the tubulin lattice of the A-tubule of the doublet (blue) and the 13-PF singlet (black) (29). The tubulin lattice is cut and unfurled at the seam as in *B*. Despite having the same 13-3 B-lattice as the 13-PF singlet, the A-tubule of the doublet shows a nonuniform tubulin dimer distance and Z-shift. (*D*) Plot of the dimer distance measurements among PFs in the doublet. For each PF, 6 dimer distances within the 48-nm repeating unit (illustrated in *B*) were measured and plotted as dots. Mean value (bar) with SD (error bar) for each PF are shown. (*E*) Bimodal pattern of the tubulin dimer distances. The dimer distances from PFs A11–A13 and A1–A3 of the doublet were plotted in the same longitudinal order as in the 48-nm unit. The dimer distances of PF A11 to A1 oscillate with every 2 tubulin units (~16 nm). (*F*) Luminal view of the PF ribbon region A11–A13. fMIP densities in the A11–A13 region are now colored based on its tracing and morphology. The short 16-nm filament density is colored in light blue while the longer filament density is colored in orange. Tubulins in PFs A11–A13 are colored while all other densities are transparent. Magnified views of *G*–*J* are indicated by a dashed box in *F*. (*K*) Schematic diagram of the filament density identified in the PF ribbon region. Per 48 nm, there are 3 short filaments between PFs A12 and A13 (light blue arrowheads) and there is 1 short filament (light blue arrowheads) and 1 longer filament (orange arrowhead) between PFs A11 and A12.

from sea urchin sperm was found to form spring-like structure upon separating from the flagella (21).

The PF ribbon region (PFs A1, A11–A13) shows a clear bimodal distribution with an oscillatory pattern of long and short dimer distances. Some PFs show rather uniform dimer distances such as PFs A2 and A3 (Fig. 2*E*). Specifically, PFs A11–A13 show a large difference of ~2 Å between the long and short dimer distances.

Recently published structures of singlets show that changes in the longitudinal tubulin dimer distance depend on the nucleotide states of β-tubulin (22–26). Stable singlets in GTP state have an elongated dimer distance while the less stable GDP-state singlets have a compacted dimer distance (27). In the doublet, the tubulins are in GDP state since we observed densities of GTP and GDP in the α- and β-tubulins, respectively (*SI Appendix*, Fig. S2 *E*–*G*). The averaged dimer distance of the 13-PF A-tubule of the doublet measured 83.1 Å (*SI Appendix*, Table S1), which is closer to the elongated GTP-type distance (83.95 Å) than the compacted GDP-type distance (81.8 Å) in singlets from *Sus scrofa* (25). We hypothesize that this elongated dimer distance is the result of the weaving network of the MIPs. In addition, the heterogeneity of dimer distances within and between the PFs suggest that the doublet tubulin lattice is inherently stressed by the insertion of MIPs.

Rib43a Proteins Are the fMIPs at the PF Ribbon Region. In order to investigate the molecular mechanism for the bimodal distribution, we looked at the currently known candidates for the PF ribbon-associated proteins. Three possible candidates are tektin, Rib72, and Rib43a. *Tetrahymena* lacks a homolog of tektin. The predicted secondary structure of Rib72 is inconsistent with the long α-helical fMIP densities. Therefore, the fMIPs in the PF ribbon region are unlikely to be tektin or Rib72, but rather Rib43a. *Tetrahymena* has 2 Rib43a homologs (UniProt ID: A4VDZ5, 142 amino acids and Q240R7, 280 amino acids). For convenience, we refer to the 2 *Tetrahymena* Rib43a homologs as Rib43a-S (short) (A4VDZ5) and Rib43a-L (long) (Q240R7) from now on.

Previously, both Rib43a proteins were detected in the mass spectrometry of the doublet (5). In the 0.2% sarkosyl-treated doublet, which contains mainly A-tubules, both Rib43a-S and Rib43a-L were also detected (*SI Appendix*, Fig. S3*A*). This indicates that both proteins exist in the A-tubule.

To improve the resolution of the PF ribbon region, we performed focused refinement to obtain a 4.16-Å resolved map of this region (*Materials and Methods*). By tracing the fMIP densities in the PF ribbon region, we were able to distinguish 2 unique peptide densities: a short 16-nm helical density (light blue in Fig. 2 *F*–*K*) and a long 32-nm density (orange in Fig. 2 *F*–*K*). In each 48-nm repeating unit, the fMIP-A12A13 comprises 3 copies of the short 16-nm helical density arranged in a head-to-tail fashion. The fMIP-A11A12 consists of the short 16-nm helical density (light blue in Fig. 2 *F* and *K*) and the long 32-nm filament (orange in Fig. 2 *F*–*K*). The observed secondary structures of the short and long filament densities match the secondary structure prediction of Rib43a-S and Rib43a-L, respectively (Fig. 3*A*).

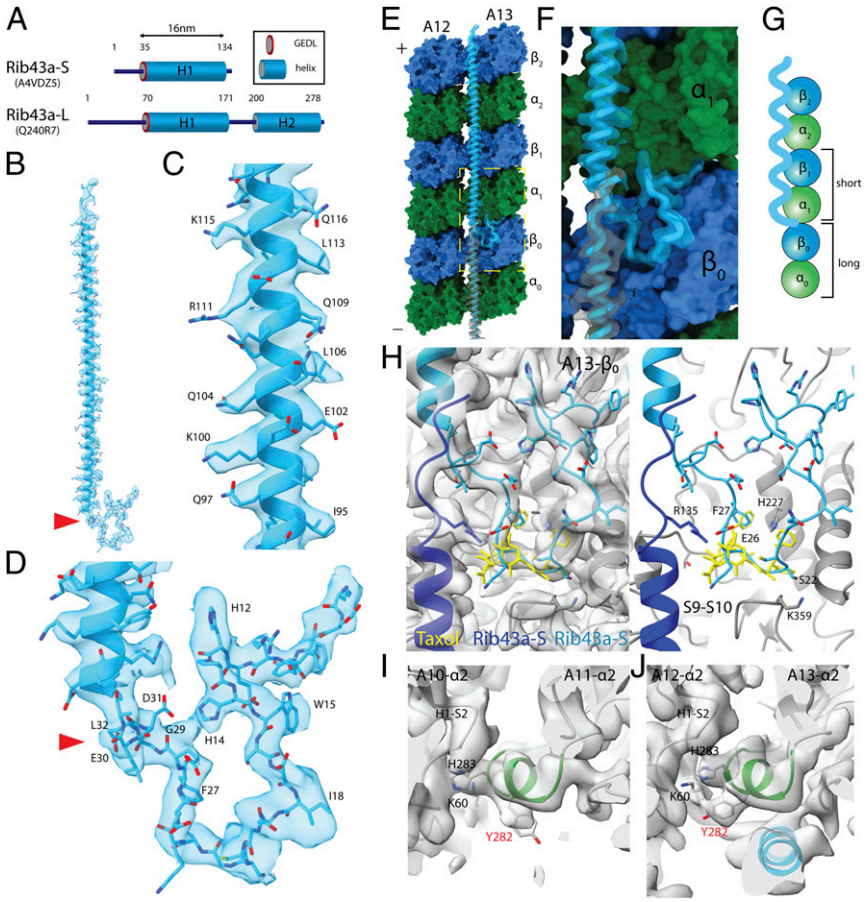

Fig. 3. Rib43a leads to the bimodal distance in the PF regions. (*A*) Secondary structure prediction of Rib43a-S and Rib43a-L. Only the large stretch of α-helices more than 20 residues from the structure prediction is shown. The GEDL consensus sequence is a conserved region of Rib43a (PFAM PF05914). (*B*) Model of the Rib43a-S inside its segmented density. (*C* and *D*) Magnified views of the helical region (*C*) and the N-terminal region (*D*) of Rib43a-S. The location of the GEDL motif is shown by the red arrowheads in *B* and *D*. (*E*) Model of Rib43a binds to the PF pair A12/A13. Yellow dashed box shows the magnified view in *F*. (*F*) The N terminus of Rib43a-S inserts into the interdimer interface in PF A13. (*G*) Schematic model of how Rib43a-S binds to the PF leading to the bimodal dimer distance pattern. (*H*) Superimposed views of taxol (PDB: 5SYF, yellow) and Rib43a-S with map (*Left*) and without map (*Right*) show similar topology. R135 in the C terminus of the lower Rib43a-S (dark blue) might interact with E26 of the N terminus of the upper Rib43a-S (light blue) in a head-to-tail dimerization mechanism. (*I* and *J*) M-loop conformations in the lateral interaction with Rib43a (PFs A12 and A13) and without (PFs A10 and A11). The side chain of Y282 adopts a different conformation in the presence of Rib43a, potentially due to steric clash. In this conformation, Y282 might interact with K60 of the neighboring α-tubulin.

Rib43a-S is composed of a continuous stretch of α-helix of about 100 amino acids, referred to as the H1 region, while Rib43a-L contains 2 long stretches of α- helices of about 100 and 80 amino acids each (H1 and H2), connected by a linker region (Fig. 3*A*).

We performed de novo modeling of the short and long filament densities using the sequences of Rib43a-S and Rib43a-L. For Rib43-S, we were able to model almost the entire protein from residues 2 through 138. Residues 60 through 172 could only be modeled for Rib43a-L due to lower resolution. The secondary structure pattern and amino acid side chains unambiguously match the density signature (Fig. 3 *B–D* and *SI Appendix*, Fig. S2 *C* and *D*). Therefore, we confirm that per 48-nm repeat, the fMIPs in the PF ribbon region consist of 4 copies of Rib43a-S and 1 copy of Rib43a-L (Fig. 2*K*).

Rib43a Recognizes β-Tubulin and Induces the Bimodal Dimer Distance. The N terminus of the Rib43a-S inserts into the intertubulin dimer interface, in between helix H2 of β-tubulin and T7 loop of α-tubulin (Fig. 3 *E–G*). This leads to a longer dimer distance every 2 tubulin dimers in PF A13 and consequently, the bimodal pattern mentioned above. In addition, residue Y8 from Rib43a-S seems to interact with GDP of β-tubulin (*SI Appendix*, Fig. S3*F*). The N terminus of the Rib43a-L does not insert into the interdimer interface but instead folds back onto helix H1 (Fig. 2*H* and *SI Appendix*, Fig. S3*C*). We also observed densities that insert into the dimer interface at the N-terminal region and the linker region between H1 and H2 helices of Rib43a-L (Fig. 2*H* and *SI Appendix*, Fig. S3*E*).

The consensus sequence GEDL of the Rib43a family is located at the N terminus of helix H1 of both proteins (Fig. 3 *A* and *D* and *SI Appendix*, Fig. S3*J*). This region inserts into the S9–S10 loop of β-tubulin, which comprises the taxane-binding pocket (28) (Fig. 3 *D* and *H* and *SI Appendix*, Fig. S3 *H* and *I*). In α-tubulin, the S9–S10 loop is longer and would prevent the binding of Rib43a-S and Rib43a-L (*SI Appendix*, Fig. S2*A*). Therefore, we can conclude that the conserved motif GEDL of Rib43a is a β-tubulin binding motif at the taxane-binding pocket. The main chain of residues 21 through 27 of Rib43a-S has a similar topology to the anticancer drug taxol, which binds at the taxane-binding pocket (Fig. 3*H*). In particular, the benzyl of F27 of Rib43a-S has a similar conformation to the 2-benzyol of taxol (28). Although this F27 residue is not present in Rib43a-L, it is conserved in the Rib43a family (*SI Appendix*, Fig. S3*J*). Taxol selectively binds to β-tubulin and stabilizes the lateral interaction

in the microtubule (28). Therefore, it is possible that the binding of Rib43a-S to the tubulin lattice might have a similar stabilizing effect.

The helical region of Rib43a spans the M-loop of 2 longitudinal tubulin dimers. In the presence of Rib43a, the side chain of Y282 of α_1 and α_2-tubulins adopts a rotamer conformation at about a 90-degree rotation from its normal position (Fig. 3 *I* and *J*). This rotamer conformation is observed in all M-loops of α-tubulin in the presence of Rib43a. The conformation of Y282 in the absence of Rib43a such as PFs A10/A11 is consistent with what is observed in singlets (23). In the PF ribbon region (A11/A12 and A12/A13), the normal conformation of Y282 will result in steric clash with the helices H1 and H2 of Rib43a. Therefore, it has to adopt a different rotamer conformation. This conformation might allow Y282 to interact with K60 from the H2–S3 loop of the neighboring α-tubulin, leading to a stronger lateral interaction. This observation suggests that Rib43a may play a role in restricting PF curvatures, consistent with the low curvatures observed in the PF pairs A11/A12 and A12/A13 (5).

With the extensive binding interface of both the N-terminal and the α-helical regions, we expect that Rib43a-S stabilizes the tubulin lattice. To test that hypothesis, we performed molecular dynamics (MD) simulations of a short PF consisting of 3 tubulin dimers with and without Rib43a-S (*SI Appendix*, Fig. S3 *K–N* and Movies S3 and S4). First, we compared the free energy at the interdimer interfaces to assess the effect of Rib43a-S on stability. The binding of the N terminus of Rib43a-S greatly shifts the free energy of the interdimer interaction to a lower state, i.e., higher stability (*SI Appendix*, Fig. S3*L*). Although the effect of the α-helical region on stability is rather mild (*SI Appendix*, Fig. S3*M*), this stabilization effect would be much stronger in vivo with the consecutive head-to-tail arrangement of Rib43a-S along the PF ribbon region. This is consistent with previous biochemical studies showing that the PF ribbon region is the most stable part of the doublet (7). Next, we examined the effect of Rib43a-S on the elasticity of the PF. Without Rib43a-S, the free energy increases (less stable) at higher vibration angles (*SI Appendix*, Fig. S3*N*). In the presence of Rib43a-S, the PF maintains a low free energy even at higher vibration angles. This result demonstrates that Rib43a-S makes the PF more elastic, rather than rigid.

Removal of Some MIPs Impacts the Compaction State and Curvature of the Doublet. We wanted to investigate whether removing MIPs would impact the tubulin lattice. Using micrographs of sonicated and sarkosyl-treated fractions, we obtained 2 types of A-tubule maps: sonicated and sarkosyl A-tubules at 4.4- and 4.9-Å resolution,

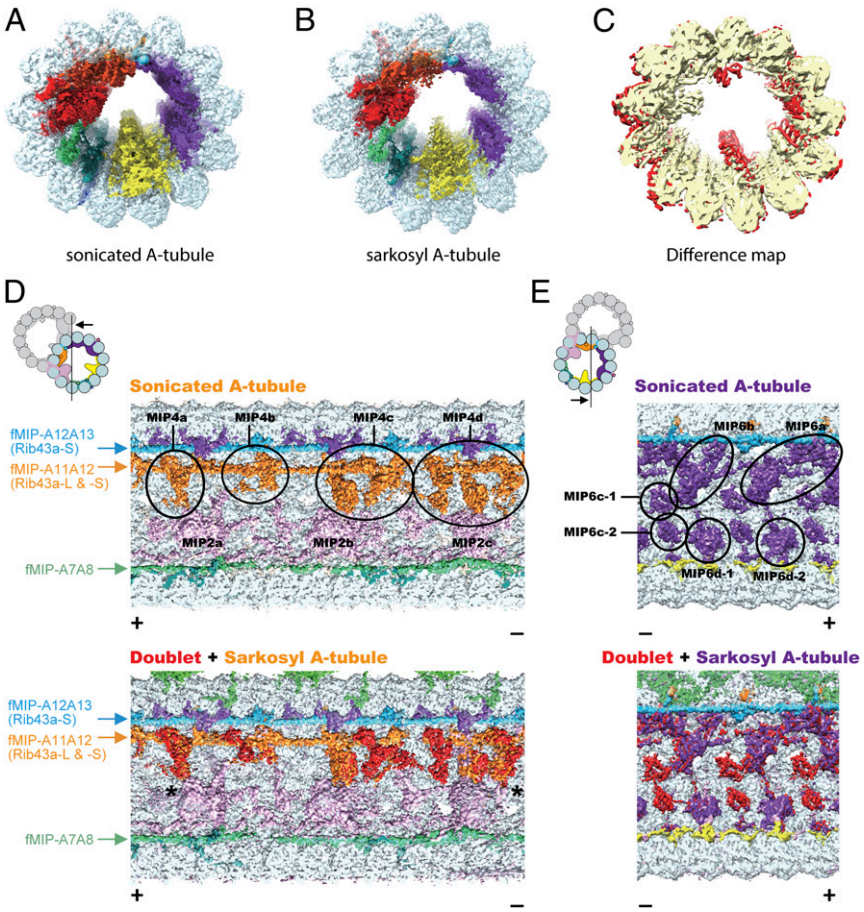

Fig. 4. Sarkosyl treatment removes some MIPs from the doublet. (*A* and *B*) Surface renderings of the sonicated A-tubule (*A*) and sarkosyl A-tubule (*B*) maps. (*C*) Difference map between the sonicated and sarkosyl A-tubule maps. Superimposition of the 2 maps reveals the missing MIP densities in the sarkosyl A-tubule map (red regions). Parts of the MIP2 and MIP6 are missing in the sarkosyl A-tubule map. (*D* and *E*) Sonicated A-tubule map (*Top*) and the overlap of doublet and sarkosyl A-tubule maps (*Bottom*). The MIP4 and MIP6 regions of the doublet (red) are mapped onto corresponding regions from the sarkosyl A-tubule map (MIP4 in orange and MIP6 in purple). The views are indicated in the illustrations on the *Top Left*. Remaining fMIPs are indicated on the side. The coloring of MIP2 and MIP4 is different from other figures to avoid confusion (see the illustration for the coloring). Some densities at the MIP4 and MIP6 regions are missing after the sarkosyl treatment while the fMIPs appear intact. The slight shifts in MIP4 (indicated by asterisks) at both + and – end are due to lateral compaction of the tubulin lattice.

respectively (Fig. 4 *A* and *B*). While the sonicated A-tubule map retains all of the MIPs inside, the sarkosyl A-tubule map has missing MIP densities (Fig. 4*C*). Multiple densities at the MIP4 and parts of the MIP6 areas are affected by the sarkosyl treatment (Fig. 4 *D* and *E* and *SI Appendix*, Fig. S4 *A* and *B*). Other MIP densities inside the sarkosyl A-tubule are less-well resolved, suggesting they were partially removed or became flexible (Fig. 4*C*).

Next, we wanted to see whether the lack of the B-tubule and the MIPs impact the dimer distances. The tubulin lattice of the sonicated A-tubule is almost identical to the doublet, except for the lack of the B-tubule (*SI Appendix*, Fig. S5*A* and Table S1). The tubulin lattice of the sarkosyl A-tubule showed a significant compaction compared to the doublet (Fig. 5 *A–E*, *SI Appendix*, Fig. S4 *C–F* and Table S1, and Movie S5). The averaged dimer distance measured 81.1 Å, which is similar to a GDP-type compacted lattice (23). Therefore, this compaction can be attributed to the loss of the MIPs, but not the lack of the B-tubule. Both Rib43a-S and Rib43a-L were not removed by the sarkosyl treatment (Fig. 4*D*). Therefore, the bimodal pattern was still maintained in the sarkosyl A-tubule (*SI Appendix*, Fig. S5*A*).

In addition to the lattice compaction, we also observed changes in the inter-PF angles (Fig. 5*F* and *SI Appendix*, Fig. S5*B*). Unlike the 13-PF singlet, which forms a near perfect circle, the A-tubule of the doublet shows a squashed cross-sectional curvature with a variety of inter-PF angles (Fig. 5*F*). Compared to the doublet, the inter-PF angles from the sarkosyl A-tubule show significant changes at PF pairs A1/A2 and A12/A13 (Fig. 5*F* and *SI Appendix*, Table S3). The MIPs are missing at these PF pairs accordingly (Fig. 4 *C–E*). The PF pair A12/A13 of the sarkosyl A-tubule, where several MIP4 densities are lost, shows the largest change of angle (Fig. 5*F* and *SI Appendix*, Fig. S5*B*). The lateral curvature between PF pairs A12/A13 of the doublet is equivalent to the curvature of a 22-PF singlet. This curvature is energetically unfavorable, as 11 to 16 PF singlets are generally formed by in vitro reconstitution (29). With the loss of MIP4, the curvature shifts toward a more relaxed conformation comparable to an 18-PF singlet (Fig. 5 *F–H*). PF pair A9/A10 also shows a slight change in the angle without any MIPs missing (Fig. 5*F*). This is the location of the seam (5) where the lateral interaction is the weakest (23). Thus, this slight angle change could be the result of the tubulin lattice accommodating the local angle changes.

Discussion

In this paper, the ex vivo structure of the doublet offers insight into the structural intricacies and complex interplay between MIPs and the tubulin lattice. Our results are the direct evidence that the MIPs influence the tubulin lattice architecture.

The MIPs work in a coordinated fashion to keep the doublet in a stable and squashed cross-section. This likely facilitates the specific and proper formation of the B-tubule (5). The network

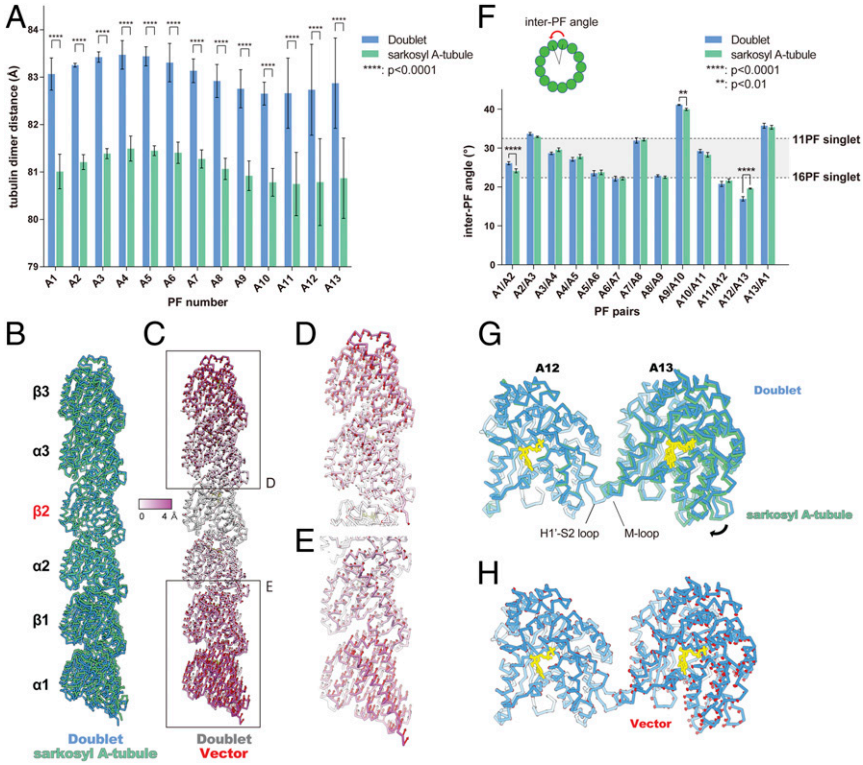

Fig. 5. Longitudinal tubulin lattice length and curvature are regulated by the MIPs. (*A*) Plot of tubulin dimer distances from doublet and the sarkosyl A-tubule. Mean values with SD for each PF are shown. The average value of each PF from the sarkosyl A-tubule shows a lateral compression of ~2 Å. Statistical analysis was performed by 2-way ANOVA, Bonferroni post hoc test (see also *SI Appendix*, Table S2). (*B*) Comparison of tubulin models refined in PF-A12 from doublet (blue) and sarkosyl A-tubule (green) showing a longitudinal compaction after missing some MIPs. Models were aligned by β2-tubulin. (*C*) Tubulin models of PF-A12 from the doublet are colored according to the degree of displacement. Vectors of the Cα displacement toward the sarkosyl A-tubule model are shown in red. (*D* and *E*) Close-up views of the tubulins from the periphery with vectors. (*F*) Plot of inter-PF angles in the doublet and sarkosyl A-tubule. Inter-PF angles were measured as shown in the schematic diagram on *Top* and mean values were plotted (see also *SI Appendix*, Fig. S5C and Table S3). Error bars represent SD. Two-way ANOVA, Bonferroni post hoc test was performed to compare the mean values. PF pairs with *P* values smaller than 0.01 are highlighted by asterisks (see also *SI Appendix*, Table S4). The gray area in the plot represents the PF pair angles commonly seen for in vitro reconstituted singlets (29). (*G*) Alignment of the models of PF pair A12/A13 from the doublet (blue) and sarkosyl A-tubule (green) based on the tubulin unit of PF-A12 reveals ~3° difference in rotation (black arrow). (*H*) The model of PFs A12/A13 from the doublet with the vectors (red) of the displacement of Cα compared to the sarkosyl A-tubule model. Nucleotides, yellow.

of MIPs prevents the loss of tubulin and spontaneous breakage by weaving into the tubulin lattice as an integrated layer (Fig. 6*A*). For a singlet, mechanical stress from repeated cycles of bending and release is shown to induce local damage (30). Motile cilia are under even higher mechanical stress due to high-frequency beating. Nevertheless, they are protected by the weaving network of MIPs. The doublet has been in vitro reconstituted from tubulin that have its flexible C terminus cleaved by subtilisin (31). This suggests that the MIPs can limit the C-terminal conformation in vivo for the initial assembly of the B-tubule. Therefore, the MIPs might play an important role in facilitating the assembly of the doublet.

We also reveal that 2 Rib43a homologs, Rib43a-S and Rib43a-L, are the fMIPs in the PF ribbon region. By performing MD simulation, we gained insight into how Rib43a stabilizes the tubulin lattice at the molecular level. The Rib43a-S induces the bimodal distance in the ribbon region by inserting into the interdimer interface every 2 dimers. Both Rib43a proteins bind consecutively to form a 48-nm fMIP-A11A12. In *Chlamydomonas* and other species, Rib43a exists as a ~43-kDa protein, with a secondary structure prediction of 3 long helices (equivalent to roughly 48 nm in length). Therefore, Rib43a might be the inside molecular ruler for the 48-nm periodicity of the doublet lumen, a role similar to the outside molecular ruler, FAP59 and FAP172 (19). Previously, tektin was proposed to regulate the complex spacing inside the doublet (10, 32). However, as tektin is not present in *Tetrahymena*, it is likely that Rib43a is the primary inside ruler. It might then act as an assembly scaffold with specific binding domains for recruiting other MIPs and establishing distinct periodicities. In addition, the tight interaction of the Rib43a-S to the tubulin lattice suggests that it might be coassembled with tubulin during ciliogenesis.

The taxane-binding pocket is known to be used by small molecules, such as paclitaxel, zampanolide (28), and epothilone A (33). Previously, tau was reported to bind to the taxane-binding pocket by visualization of nanogold conjugation (34); however, this finding was not reproduced in a more recent high-resolution study (35). Our work provides direct evidence that a native protein is using the taxane-binding pocket to stabilize the tubulin lattice. In addition, taxol is shown to induce deformation in the microtubule wall (28). This effect can also be exerted by Rib43a to induce low curvatures at the PF ribbon region. There could be other proteins utilizing the same approach to stabilize the microtubule lattice not only in cilia but also in cytoplasmic microtubules. Identifying such proteins using bioinformatic approaches can be a first step toward understanding how microtubules are stabilized by regulatory proteins.

Recent studies demonstrate that the elongation and compaction of the tubulin lattice plays an important role in the dynamic instability of singlet microtubules (22–26). Microtubule-associated proteins can have a direct effect on the lattice compaction and, hence, microtubule dynamics (26). Our results suggest that the MIPs, in particular Rib43a, function as a molecular jack to regulate the tubulin lattice in an elongated state (Fig. 6*B*). This points to a common mechanism where the lattice maintenance is used to regulate stability and properties such as ciliary waveform. A previous study showed that doublets purified from sea urchin sperm flagella form spring-like structures, the shape of which, depends on the pH or calcium ion concentration (21). This implies that the degree of inherent tension inside the doublet can be tweaked by external cues. Coincidentally, Rib72a (12) and FAP85 (36) are 2 MIP candidates that have calcium-binding domains. Thus, MIPs could manipulate tubulin conformations as a way to modify the rigidity and elasticity of the doublet and, thus, ciliary bending (Fig. 6*B*).

Since Rib43a induces a conformational change in the M-loop region, it can act as a molecular wedge to lock the PF pairs at a low curvature (Figs. 5*F* and 6*C*). Conversely, there may be MIPs, which act as a molecular linker, which results in a high curvature (Fig. 6*C*). For example, MIP2 can be a molecular linker as it was shown to insert into the PF pair A9/A10 (5), which has a significantly high curvature (Fig. 5*F*). Recently, it was reported that the microtubule-binding domain of axonemal dynein DNAH7 could induce large distortions in the microtubule cross-sectional curvature (37). This suggests that there is a preferential curvature for the microtubule-binding domain of DNAH7. Distortions in the doublet cross-sectional curvature caused by MIPs might then facilitate the axonemal dynein to interact with specific regions.

Herein, we propose a lattice centric model for the cilia in which the tubulin lattice serves as a platform to integrate the binding signals of the MIPs and outer proteins. Binding of the MIPs leads to the local and global lattice rearrangement, which affects the affinity of the outer proteins like axonemal dyneins and radial spokes. This allows the assembly of the complex axoneme in an orderly fashion (1) for proper ciliary function. The unique dimer distances among different PFs and the inside-to-outside connections can influence the binding affinity of the intraflagellar transport motors to the A- or B-tubules selectively (2).

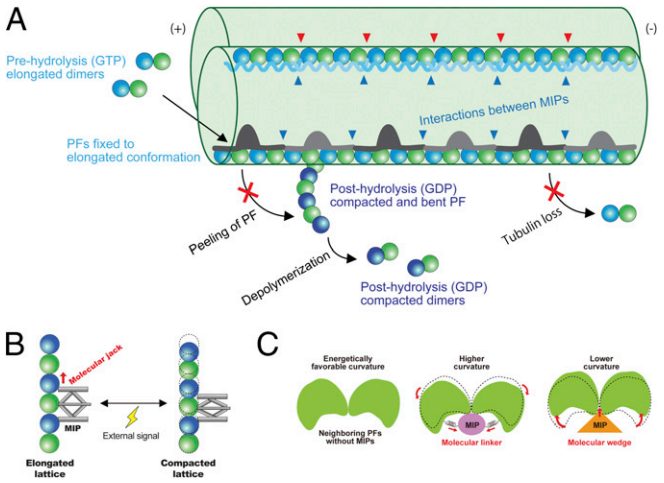

Fig. 6. Model of stabilization mechanisms of the doublet tubulin lattice by MIPs. (*A*) Model of the impacts of the MIPs on the doublet. First, elongated tubulin dimers in GTP prehydrolysis state are incorporated into the tubulin lattice. This elongated and stable conformation is fixed after assembly into the lattice through the interactions with the MIPs. The network of MIPs (blue arrowheads) also holds the tubulin lattice from the inside to prevent the loss of tubulin or breakage. At the plus end, MIPs prevent the peeling of PFs and depolymerization by keeping PFs in a stable and elongated conformation. Hence, the doublet is stabilized by the MIPs at several different levels to ensure that it can withstand the mechanical stress and prevent catastrophic events for the cilia. Some MIPs, such as Rib43a, have insertions into the tubulin lattice (red arrowheads), causing the larger interdimer gap and bimodal dimer distance. (*B*) Schematic diagram of the function of the MIPs in regulating tubulin lattice length. Some MIPs work as a molecular jack to keep the tubulin lattice elongated. External signals could change the MIP property and thereby the tubulin lattice. (*C*) MIPs regulate the angles between PFs. Without MIPs, tubulin lattice takes an energetically favorable curvature. Some MIPs work as molecular linkers, which hold adjacent tubulin pairs together so that it will take a higher curvature such as in the PFs A9/A10. Other MIPs, in particular, Rib43a work as molecular wedges and open the PF pairs and induce a lower curvature.

Materials and Methods

Sample Preparation. *Tetrahymena* doublet fragments were prepared as in Ichikawa et al. (5) (*SI Appendix*, Fig. S1 *A* and *B*). In brief, *Tetrahymena* cells (SB255 strain) were cultured in 1 L of SPP media (1% proteose peptone No. 3, 0.2% glucose, 0.1% yeast extract, 0.003% EDTA ferric sodium salt [Fe-EDTA]). Cilia were isolated by dibucaine method (38) and resuspended in cilia final

buffer (CFB) (50 mM 4-(2-hydroxyethyl)-1-piperazineethanesulfonic acid [Hepes], pH 7.4, 3 mM $MgSO_4$, 0.1 mM ethylene glycol tetraacetic acid [EGTA], 0.5% Trehalose, 1 mM DTT) containing 1 mM phenylmethylsulfonyl fluoride (PMSF). Cilia were demembraned by adding Nonidet P-40 (final concentration 1.5%), split by adding ATP (final concentration 0.4 mM), and incubated in CFB containing 0.6 M NaCl for 30 min on ice twice to remove dyneins. *Tetrahymena* doublets were dialyzed against low salt buffer (5 mM Hepes, pH 7.4, 1 mM DTT, 0.5 mM EDTA) to deplete radial spokes, and then, fragmented by sonication and resuspended in CFB containing 0.6 M NaCl to avoid aggregation of doublet fragments. After sonication, the sample contained short doublet fragments and A-tubule-only fragments.

For the sarkosyl A-tubule, the doublets after twice 0.6 M NaCl treatment and dialysis were incubated with CFB containing 0.2% sarkosyl to remove the B-tubule for 10 min on ice. Sonication was not performed on this sample prior to electron microscopy.

Mass Spectrometry. In previous work, we performed in-gel digestion of stacking gel of the doublet preparation (5) using a standard method (39). In this study, we cut gel bands from different positions in the SDS gel of the sarkosyl A-tubule sample and performed in-gel digestion. The samples were analyzed using a Thermo Orbitrap Fusion mass spectrometer with HCD sequencing all peptides with a charge of 2+ or greater. The raw data were searched against the *Tetrahymena* proteins from UniProt and then visualized by Scaffold Viewer 4.4.8 (Proteome Sciences) for statistical treatment and data visualization.

Electron Microscopy. A total of 3.5 μL of the sample of fragmented doublets (~4 mg/mL) or the sarkosyl A-tubule (~500 μg/mL) was applied to a glow-discharged holey carbon grid (Quantifoil R2/2), blotted, and plunged into liquid ethane using Vitrobot Mark IV (Thermo Fisher Scientific) at 25 °C and 100% humidity with a blot force of 3 or 4 and a blot time of 5 s. Movies of 7 frames were obtained on a Titan Krios (Thermo Fisher Scientific) equipped with a Falcon II camera at 59,000 nominal magnification. The calibrated pixel size was 1.375 Å/pixel. Both datasets for the doublet and sarkosyl A-tubule were obtained with a total dose of ~30 to 45 electrons/$Å^2$. The defocus range was set to between −1.2 and −3.8 μm.

Image Processing. The movies were motion corrected and dose weighted using MotionCor2 (40) implemented in Relion3 (41), and the contrast transfer function parameters were estimated using Gctf (42). After discarding micrographs with apparent drift and ice contamination and bad contrast transfer function estimation, 7,838 micrographs for doublet and 5,179 micrographs for sarkosyl treated A-tubule were used, respectively. The filaments (doublet and A-tubule) were picked using e2helixboxer (43). Since the preparation of doublet yielded both doublets and A-tubules (*SI Appendix*, Fig. S1*A*), we also picked the A-tubule from the micrographs for the doublet.

The particles of 512 × 512 pixels were initially picked with 16-nm periodicity and prealigned using a modified version of the iterative helical real space reconstruction script (44) in SPIDER (45) to work with nonhelical symmetry. After that, the particles were separated into 3 classes by multiple reference projection matching by Frealign (46). The 3 classes above are: 1) the 48-nm structures of the doublet from Ichikawa et al. (5); 2) the 16-nm shifted structure in the longitudinal axis to the plus end; and 3) the minus end. This multiple reference projection matching allowed us to sort the particles belonging to each 48-nm class. The particles were then reextracted in Relion and rescaled to a pixel size of 1.750 Å/pixel for faster processing. The aligned parameters were converted to Relion star file format for local refinement. In summary, 60,386 and 36,375 particles for doublet and A-tubule yielded maps of 4.7 and 4.8 Å resolution, respectively. The 40,850 particles for sarkosyl A-tubule yielded a 5.2-Å resolution map. After iterative per-particle-defocus refinement and Bayesian polishing in Relion3, the resolutions of the doublet, sonicated A-tubule, and sarkosyl A-tubule maps were improved to 4.3, 4.4, and 4.9 Å, respectively. The doublet and sonicated A-tubule maps were sharpened using Relion3 with a B-factor of −190 and −179 $Å^2$, respectively.

Since the sarkosyl A-tubule map exhibited a slightly preferred orientation and resolution heterogeneity in the structure, we performed a local restoration and local sharpening to reduce artifact and restore connectivity from preferred orientation and resolution heterogeneity (*SI Appendix*, Fig. S1 *G–J*). To ensure the local restoration and local sharpening did not alter the maps, we performed the local restoration and local sharpening of the doublet and A-tubule. There were no artifacts observed compared with global sharpening.

To improve the resolution of the PF ribbon region, we performed a focused refinement by using a mask covering the PF ribbon region and also PF A9, A10, and B1. The resulting map has a resolution of 4.16 Å.

Local resolution estimation was performed using Monores (47) (*SI Appendix*, Fig. S1*F*).

Difference Map. To reliably identify the densities missing in the sarkosyl A-tubule, the unsharpened maps of the sonicated and sarkosyl A-tubule were filtered to 6 Å before performing difference mapping in Chimera. After the subtraction, the regions of difference were mapped onto the sarkosyl A-tubule map as shown in Fig. 4*C*.

Modeling. An α- and β-tubulin model of *Tetrahymena* (UniProt sequence α: P41351, β: P41352) was constructed by homology modeling in Modeler v9.19 (48) using multiple models: 1TUB, 4U3J, 1TVK, 3JAR, and 5SYF as templates and for restraints generation for atomic refinement. The restraints were generated in ProSmart (49) and the refinement was conducted iteratively until convergence in Refmac5 (50). The model was validated using comprehensive validation for cryo-EM in Phenix v1.14 (51).

In order to model Rib43a-S, the candidate density in the ribbon region was traced in Coot v0.8.9.1 (52) and found to have approximately the same length as Rib43a-S (UniProt code: A4VDZ5). The secondary and tertiary structure predictions of Rib43a-S, using JPred v4 (53) and I-TASSER (54), respectively, were analyzed and confirmed to correspond to the secondary structure regions of the density map: an α-helical region and a coiled region. In order to find the correct amino acid registry, the main bulky residues of the sequence were fitted in the map in both directions of the C- and N-termini and the fit of the remainder of the sequence was inspected. The final model matches with the predicted coiled N terminus and α-helical C terminus with unambiguous density signature agreement in the highlighted ribbon region.

The same methodology was followed for building Rib43a-L. Both models were refined and validated in Refmac5 and Phenix, respectively, as described for the *Tetrahymena* α/β-tubulin model.

Intra and Interdimer Distance Measurement. The α- and β-tubulin could be clearly distinguished in the maps using the S9–S10 loop (*SI Appendix*, Fig. S2 *A–C*). We docked in the atomic models of the α- and β-tubulins in the map separately. The intradimer distance was measured as the distance between the N9 of GTP in the α-tubulin and GDP in the β-tubulin of the same tubulin dimer in Chimera. The interdimer distance was measured between N9 of GDP of the α-tubulin and GDP in the β-tubulin in the next tubulin dimer. The dimer distance was calculated as a sum of the intra- and interdimer distances.

PF Pair Rotation Angle (Lateral Curvature) Measurement. The lateral curvature can be represented by the lateral rotation angle between each PF pair. The rotation angles and Z-shift between PF pairs were measured using the "measure" command from University of California, San Francisco Chimera (55) according to Ichikawa et al. (5).

Secondary Structure Prediction. Secondary structure prediction of Rib43a-S and Rib43a-L was done using the JPRED4 prediction server (53).

Coarse-Grained MD Simulation. Based on the atomic structures of the 3 tubulin dimers and Rib43a-S, coarse-grained MD simulation was performed. Since we were able to model almost the entire region of Rib43a-S, this isoform was used for the simulation. In the coarse-grained model, each amino acid was represented as a single bead located at its C position as shown in *SI Appendix*, Fig. S3*K*. For observing dynamics, we used the energy function AICG2+ (56, 57). In the AICG2+, the original reference structure was assumed as the most stable structure, and parameters could be modified to represent the interactions in the reference structure. We performed coarse-grained MD on 3 tubulin dimers with and without Rib43a. Four residues (T382, K401, E415, and E433) from the α-tubulin at the minus end side (chain α_0 in *SI Appendix*, Fig. S3*K*) were anchored for convenience of the analysis. It is known that the intradimer interaction is much stronger than the interdimer interaction. To replicate this feature in our simulation, we set interdimer's nonlocal native interacting force to 0.1 times the original value while that of intradimer was left as the original value (1.0 times the original value). Then, we performed the simulation 30 times with and without Rib43a-S using the CafeMol package version 2.1 (58). Each MD simulation took 10^7 MD steps, with 1 MD step roughly corresponding to ~1 ps. The MD simulations were conducted by the underdamped Langevin dynamics at a temperature of 300 K. We set the

friction coefficient to 0.02 (CafeMol unit), and default values in CafeMol were used for other parameters.

Visualization. The maps and models were segmented, colored, and visualized using Chimera (55) and ChimeraX (59).

Data Availability. The electron microscopy maps of the doublet, sonicated A-tubule, and sarkosyl A-tubule are available in the EM Data Bank (https://www.emdataresource.org) under accession numbers EMD-20602, EMD-20603, and EMD-20606. The coordinates of tubulin lattice, Rib43a-S, and Rib43a-L are available in PDB under accession number 6U0H, 6U0T, and 6U0U.

The dataset analyzed and raw data of the measurements are available from the corresponding author upon fair request.

ACKNOWLEDGMENTS. We thank Gary Brouhard, Susanne Bechstedt, Joaquin Ortega, and Alba Guarne for helpful discussion and Kelly Sears for editing the manuscript. We thank the Facility for Electron Microscopy Research of McGill University. This work was supported by grants from the Natural Sciences and Engineering Research Council of Canada (RGPIN-2016-04954), Canada Institute of Health Research (CIHR PJT-156354), the Canada Institute for Advanced Research Arzieli Global Scholars Program (to K.H.B.) and the Natural Sciences and Engineering Research Council of Canada (RGPIN-2018-04813 to J.V.). M.I. is supported by Japan Society for the Promotion of Science Overseas Research Fellowships. A.A.Z.K. is a recipient of the Al Ghurair STEM program scholarship from the Abdulla Al Gurair Foundation for Education. S.K. is supported by a JSPS Overseas Challenge Program for Young Researchers. We declare no competing financial interests.

1. K. H. Bui, T. Yagi, R. Yamamoto, R. Kamiya, T. Ishikawa, Polarity and asymmetry in the arrangement of dynein and related structures in the Chlamydomonas axoneme. *J. Cell Biol.* **198**, 913–925 (2012).
2. L. Stepanek, G. Pigino, Microtubule doublets are double-track railways for intraflagellar transport trains. *Science* **352**, 721–724 (2016).
3. M. Fliegauf, T. Benzing, H. Omran, When cilia go bad: Cilia defects and ciliopathies. *Nat. Rev. Mol. Cell Biol.* **8**, 880–893 (2007).
4. A. Akhmanova, M. O. Steinmetz, Tracking the ends: A dynamic protein network controls the fate of microtubule tips. *Nat. Rev. Mol. Cell Biol.* **9**, 309–322 (2008).
5. M. Ichikawa *et al*., Subnanometre-resolution structure of the doublet microtubule reveals new classes of microtubule-associated proteins. *Nat. Commun.* **8**, 15035 (2017).
6. M. A. Pirner, R. W. Linck, Tektins are heterodimeric polymers in flagellar microtubules with axial periodicities matching the tubulin lattice. *J. Biol. Chem.* **269**, 31800–31806 (1994).
7. J. M. Norrander, A. M. deCathelineau, J. A. Brown, M. E. Porter, R. W. Linck, The Rib43a protein is associated with forming the specialized protofilament ribbons of flagellar microtubules in Chlamydomonas. *Mol. Biol. Cell* **11**, 201–215 (2000).
8. D. Nicastro *et al*., The molecular architecture of axonemes revealed by cryoelectron tomography. *Science* **313**, 944–948 (2006).
9. D. Nicastro *et al*., Cryo-electron tomography reveals conserved features of doublet microtubules in flagella. *Proc. Natl. Acad. Sci. U.S.A.* **108**, E845–E853 (2011).
10. H. Sui, K. H. Downing, Molecular architecture of axonemal microtubule doublets revealed by cryo-electron tomography. *Nature* **442**, 475–478 (2006).
11. G. Pigino *et al*., Comparative structural analysis of eukaryotic flagella and cilia from Chlamydomonas, Tetrahymena, and sea urchins. *J. Struct. Biol.* **178**, 199–206 (2012).
12. D. Stoddard *et al*., Tetrahymena RIB72A and RIB72B are microtubule inner proteins in the ciliary doublet microtubules. *Mol. Biol. Cell* **29**, 2566–2577 (2018).
13. M. Owa *et al*., Inner lumen proteins stabilize doublet microtubules in cilia and flagella. *Nat. Commun.* **10**, 1143 (2019).
14. M. Ichikawa, K. H. Bui, Microtubule inner proteins: A meshwork of luminal proteins stabilizing the doublet microtubule. *BioEssays* **40**, 1700209 (2018).
15. S. M. King, Axonemal protofilament ribbons, DM10 domains, and the link to juvenile myoclonic epilepsy. *Cell Motil. Cytoskeleton* **63**, 245–253 (2006).
16. R. Ryan *et al*., Functional characterization of tektin-1 in motile cilia and evidence for TEKT1 as a new candidate gene for motile ciliopathies. *Hum. Mol. Genet.* **27**, 266–282 (2018).
17. A. Ta-Shma *et al*., A human laterality disorder associated with a homozygous WDR16 deletion. *Eur. J. Hum. Genet.* **23**, 1262–1265 (2015).
18. Z. S. Kangkang Song *et al*., Structure of the ciliary axoneme at nanometer resolution reconstructed by TYGRESS. BioRvix:10.1101/363317 (6 July 2018).
19. T. Oda, H. Yanagisawa, R. Kamiya, M. Kikkawa, A molecular ruler determines the repeat length in eukaryotic cilia and flagella. *Science* **346**, 857–860 (2014).
20. R. W. Linck, Flagellar doublet microtubules: Fractionation of minor components and alpha-tubulin from specific regions of the A-tubule. *J. Cell Sci.* **20**, 405–439 (1976).
21. T. Miki-Noumura, R. Kamiya, Conformational change in the outer doublet microtubules from sea urchin sperm flagella. *J. Cell Biol.* **81**, 355–360 (1979).
22. G. M. Alushin *et al*., High-resolution microtubule structures reveal the structural transitions in αβ-tubulin upon GTP hydrolysis. *Cell* **157**, 1117–1129 (2014).
23. R. Zhang, G. M. Alushin, A. Brown, E. Nogales, Mechanistic origin of microtubule dynamic instability and its modulation by EB proteins. *Cell* **162**, 849–859 (2015).
24. S. W. Manka, C. A. Moores, The role of tubulin-tubulin lattice contacts in the mechanism of microtubule dynamic instability. *Nat. Struct. Mol. Biol.* **25**, 607–615 (2018).
25. R. Zhang, B. LaFrance, E. Nogales, Separating the effects of nucleotide and EB binding on microtubule structure. *Proc. Natl. Acad. Sci. U.S.A.* **115**, E6191–E6200 (2018).
26. R. Zhang, J. Roostalu, T. Surrey, E. Nogales, Structural insight into TPX2-stimulated microtubule assembly. *eLife* **6**, e30959 (2017).
27. S. W. Manka, C. A. Moores, Microtubule structure by cryo-EM: Snapshots of dynamic instability. *Essays Biochem.* **62**, 737–751 (2018).
28. E. H. Kellogg *et al*., Insights into the distinct mechanisms of action of taxane and non-taxane microtubule stabilizers from cryo-EM structures. *J. Mol. Biol.* **429**, 633–646 (2017).
29. H. Sui, K. H. Downing, Structural basis of interprotofilament interaction and lateral deformation of microtubules. *Structure* **18**, 1022–1031 (2010).
30. L. Schaedel *et al*., Microtubules self-repair in response to mechanical stress. *Nat. Mater.* **14**, 1156–1163 (2015).
31. M. Schmidt-Cernohorska *et al*., Flagellar microtubule doublet assembly in vitro reveals a regulatory role of tubulin C-terminal tails. *Science* **363**, 285–288 (2019).
32. J. M. Norrander, C. A. Perrone, L. A. Amos, R. W. Linck, Structural comparison of tektins and evidence for their determination of complex spacings in flagellar microtubules. *J. Mol. Biol.* **257**, 385–397 (1996).
33. A. E. Prota *et al*., Molecular mechanism of action of microtubule-stabilizing anticancer agents. *Science* **339**, 587–590 (2013).
34. S. Kar, J. Fan, M. J. Smith, M. Goedert, L. A. Amos, Repeat motifs of tau bind to the insides of microtubules in the absence of taxol. *EMBO J.* **22**, 70–77 (2003).
35. E. H. Kellogg *et al*., Near-atomic model of microtubule-tau interactions. *Science* **360**, 1242–1246 (2018).
36. J. Kirima, K. Oiwa, Flagellar-associated protein FAP85 is a microtubule inner protein that stabilizes microtubules. *Cell Struct. Funct.* **43**, 1–14 (2018).
37. S. E. Lacey, S. He, S. H. W. Scheres, A. P. Carter, Cryo-EM of dynein microtubule-binding domains shows how an axonemal dynein distorts the microtubule. *eLife* **8**, e47145 (2019).
38. G. B. Witman, Isolation of Chlamydomonas flagella and flagellar axonemes. *Methods Enzymol.* **134**, 280–290 (1986).
39. A. Shevchenko, H. Tomas, J. Havlis, J. V. Olsen, M. Mann, In-gel digestion for mass spectrometric characterization of proteins and proteomes. *Nat. Protoc.* **1**, 2856–2860 (2006).
40. S. Q. Zheng *et al*., MotionCor2: Anisotropic correction of beam-induced motion for improved cryo-electron microscopy. *Nat. Methods* **14**, 331–332 (2017).
41. J. Zivanov *et al*., New tools for automated high-resolution cryo-EM structure determination in RELION-3. *eLife* **7**, e42166 (2018).
42. K. Zhang, Gctf: Real-time CTF determination and correction. *J. Struct. Biol.* **193**, 1–12 (2016).
43. G. Tang *et al*., EMAN2: An extensible image processing suite for electron microscopy. *J. Struct. Biol.* **157**, 38–46 (2007).
44. E. H. Egelman, The iterative helical real space reconstruction method: Surmounting the problems posed by real polymers. *J. Struct. Biol.* **157**, 83–94 (2007).
45. J. Frank *et al*., SPIDER and WEB: Processing and visualization of images in 3D electron microscopy and related fields. *J. Struct. Biol.* **116**, 190–199 (1996).
46. N. Grigorieff, FREALIGN: High-resolution refinement of single particle structures. *J. Struct. Biol.* **157**, 117–125 (2007).
47. J. L. Vilas *et al*., MonoRes: Automatic and accurate estimation of local resolution for electron microscopy maps. *Structure* **26**, 337–344.e4 (2018).
48. B. Webb, A. Sali, Protein structure modeling with MODELLER. *Methods Mol. Biol.* **1137**, 1–15 (2014).
49. R. A. Nicholls, F. Long, G. N. Murshudov, Low-resolution refinement tools in REFMAC5. *Acta Crystallogr. D Biol. Crystallogr.* **68**, 404–417 (2012).
50. G. N. Murshudov *et al*., REFMAC5 for the refinement of macromolecular crystal structures. *Acta Crystallogr. D Biol. Crystallogr.* **67**, 355–367 (2011).
51. P. D. Adams *et al*., PHENIX: A comprehensive python-based system for macromolecular structure solution. *Acta Crystallogr. D Biol. Crystallogr.* **66**, 213–221 (2010).
52. P. Emsley, B. Lohkamp, W. G. Scott, K. Cowtan, Features and development of Coot. *Acta Crystallogr. D Biol. Crystallogr.* **66**, 486–501 (2010).
53. A. Drozdetskiy, C. Cole, J. Procter, G. J. Barton, JPred4: A protein secondary structure prediction server. *Nucleic Acids Res.* **43**, W389–W394 (2015).
54. J. Yang *et al*., The I-TASSER suite: Protein structure and function prediction. *Nat. Methods* **12**, 7–8 (2015).
55. E. F. Pettersen *et al*., UCSF Chimera–A visualization system for exploratory research and analysis. *J. Comput. Chem.* **25**, 1605–1612 (2004).
56. W. Li, T. Terakawa, W. Wang, S. Takada, Energy landscape and multiroute folding of topologically complex proteins adenylate kinase and 2ouf-knot. *Proc. Natl. Acad. Sci. U.S.A.* **109**, 17789–17794 (2012).
57. W. Li, W. Wang, S. Takada, Energy landscape views for interplays among folding, binding, and allostery of calmodulin domains. *Proc. Natl. Acad. Sci. U.S.A.* **111**, 10550–10555 (2014).
58. H. Kenzaki *et al*., CafeMol: A coarse-grained biomolecular simulator for simulating proteins at work. *J. Chem. Theory Comput.* **7**, 1979–1989 (2011).
59. T. D. Goddard *et al*., UCSF ChimeraX: Meeting modern challenges in visualization and analysis. *Protein Sci.* **27**, 14–25 (2018).
60. H. A. Yanagisawa *et al*., FAP20 is an inner junction protein of doublet microtubules essential for both the planar asymmetrical waveform and stability of flagella in Chlamydomonas. *Mol. Biol. Cell* **25**, 1472–1483 (2014).